Fusion Science and Technology

ISSN: 1536-1055 (Print) 1943-7641 (Online) Journal homepage: http://www.tandfonline.com/loi/ufst20

Manufacturing and Testing of Multiaperture and Multichannel Grids for the Prototype Negative Ion Source for CFETR-NBI System

Yuming Gu, Jun Li, Jianglong Wei, Yahong Xie, Lizhen Liang & Chundong Hu

To cite this article: Yuming Gu, Jun Li, Jianglong Wei, Yahong Xie, Lizhen Liang & Chundong Hu (2017) Manufacturing and Testing of Multiaperture and Multichannel Grids for the Prototype Negative Ion Source for CFETR-NBI System, Fusion Science and Technology, 72:2, 148-156

To link to this article: http://dx.doi.org/10.1080/15361055.2017.1319718

Published online: 24 May 2017.

FUSION SCIENCE AND TECHNOLOGY · VOLUME 72 · 148–156 · AUGUST 2017

DOI: https://doi.org/10.1080/15361055.2017.1319718

Technical Note

Manufacturing and Testing of Multiaperture and Multichannel Grids for the Prototype Negative Ion Source for CFETR-NBI System

Yuming Gu, Jun Li, Jianglong Wei,* Yahong Xie, Lizhen Liang, and Chundong Hu

Institute of Plasma Physics, Chinese Academy of Sciences, Hefei 230031, China

Received July 22, 2016
Accepted for Publication December 5, 2016

Abstract — *A prototype negative ion source is in development toward the giant negative ion source for the China Fusion Engineering Test Reactor neutral beam injection system at the Institute of Plasma Physics, Chinese Academy of Sciences. The multiaperture and multichannel grids are the most challengeable during the construction of the prototype negative ion source. The research and development activities for the grid manufacturing method were carried out and divided into detailed design, implementation, and testing phases. Based on a special manufacturing process involving the vacuum brazing technique, some prototype grids were produced. Two prototypes have similar structures to the extraction grid of the prototype negative ion source except for the reduced number of cooling channels. A testing campaign (including dimension inspection, leak tests, thermal imaging tests, and magnetic tests) was carried out. The results demonstrate that the manufacturing process and construction technology can meet the requirements of the extraction grid and can promote the construction of other grids or components having a similar structure.*

Keywords — *Accelerator, multichannel grid, negative ion source.*

Note — *Some figures may be in color only in the electronic version.*

I. INTRODUCTION

A new fusion facility named the China Fusion Engineering Test Reactor (CFETR) is under conceptual design. CFETR is regarded as an important intermediate step between ITER and DEMO (Refs. 1 and 2). The major mission of CFETR is to demonstrate full cycle of tritium self-sustained with tritium breeding ratio ≥1.2. The neutral beam injection (NBI) is proposed to support the plasma heating and current driver of CFETR, with a beam energy of 500 keV, beam power of 20 MW (potential upgrade to 40 MW), and off-axis injection. A negative ion source (half-size ITER source and beam pulse more than 1 h) is essential at such a high beam energy to attain an acceptable neutralization efficiency. In order to gain experience on the design, manufacturing, and operation for the negative ion source of the CFETR-NBI system, Hefei utility negative ion test equipment with radio frequency (RF) source is in development at the Institute of Plasma Physics, Chinese Academy of Sciences (ASIPP).

The prototype negative ion source consists of an RF driver, expansion chamber, and negative ion accelerator,[3] as shown in Fig. 1. The RF driver was developed and tested on a small test bed at first.[4] The RF driver concept will also be used for the upgrade of the EAST-NBI positive ion source. The expansion chamber is based on the current EAST-NBI ion source,[5–8] and acts as an expansion region for negative ion production. A cesium supply system and an external magnetic filter are added to increase the negative ion beam current and suppress the coextracted electrons.[9,10] An ITER-like multiaperture grid system will be applied to the negative ion accelerator,[11] which comprises the plasma grid (PG), extraction grid (EG),

*E-mail: jlwei@ipp.ac.cn

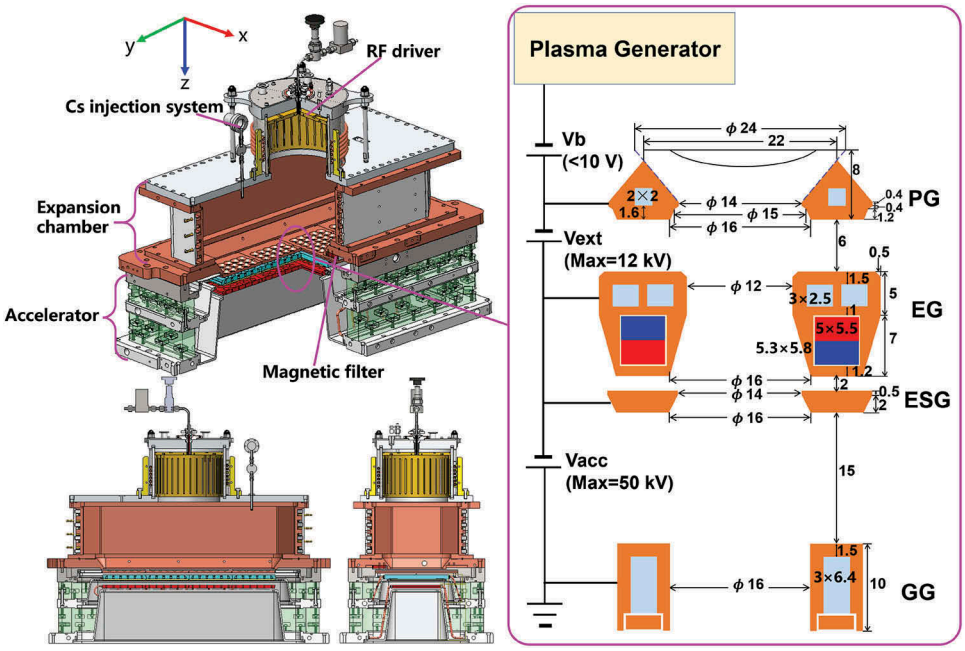

Fig. 1. (a) The three-dimensional diagram of the prototype negative ion source at ASIPP and the detailed geometry of the grid aperture. (b) In the geometry plot, the light blue rectangles represent the cooling channels, and the red and dark blue rectangle combinations represent the electron deflection magnets. Their section sizes are indicated nearby. Distance units in all the figures are mm.

electron suppression grid (ESG), and ground grid (GG). Each grid is divided into four identical segments, and each segment consists of 6 × 5 apertures. The aperture geometry of all grids is also indicated in Fig. 1. The extraction voltage between the PG and EG is up to 12 kV, and the maximum acceleration voltage between the EG and GG is 50 kV. The ESG is attached to the EG at the same electric potential in order to suppress the leakage of secondary electrons. The first target of the prototype negative ion source is long pulse (≥3600 s) generation of negative ions (H^-) in the Cs-seeded RF source. The second target is the high current density (≥350 A/m^2) extraction of the negative ion beam. The pulse duration of beam extraction is limited to 100 s.

In either the positive or negative ion source, the electrode grid system often limits the source performance.[12–14] Although the multislot grids for the EAST-NBI ion source have demonstrated a sound capability and stability, the multiaperture grids for the prototype negative ion source are quite different in terms of complex structure and some strict requirements, especially for the EG, which has a separated multichannel structure for cooling water and electron deflection magnets and has to endure long pulse of heat load. Six prototype grids (four PGs and two EGs) were designed, constructed, and tested at ASIPP. All the grids have been successfully completed. In this technical note, the manufacturing process of the prototype EG is described in detail. A testing campaign was carried out to validate the process and construction technology.

II. DESIGN OF THE EXTRACTION GRID

The EG is applied to a relatively low voltage against the PG to extract negative ions from the expansion chamber. Meanwhile, the negatively charged electrons also are extracted. If the coextracted electrons are accelerated to high energy, they will damage the grids downstream and the beamline components and also waste the capability of the high-voltage power supply. Therefore, rows of permanent magnets are embedded into the EG to filter the coextracted electrons during the extraction stage.

Generally, the coextracted electrons are deflected and dumped onto the EG top surface by the electron deflection field.[15–17] Thus, an ITER-like EG design is adopted to remove the power load (up to 40 MW/m^2 localized) effectively. Inside the EG, the cooling channels are located near the top surface, as shown in Fig. 2. Two separated cooling channels are placed between the aperture rows, attempting to gain a better heat removal.[15] The pair of cooling channels is 3 mm wide, 2.5 mm deep, and 1 mm apart. These small cooling channels collect together at two manifolds inside the grid. One

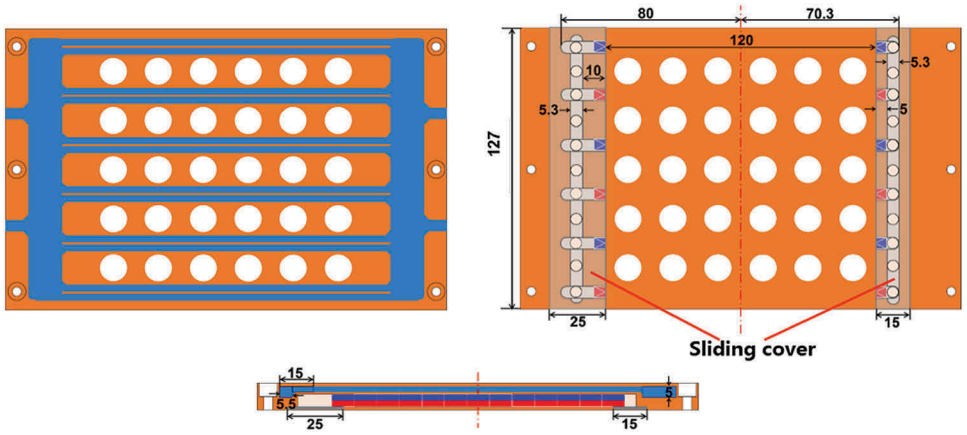

Fig. 2. The cooling scheme and magnet arrangement of the EG (top, back, and side view). The light blue rectangles represent the cooling channels, and the red and dark blue rectangle combinations represent the electron deflection magnets.

manifold connects two inlets and the other one connects two outlets.

The electron deflection magnet rows are just down from the cooling channels. The magnets can be inserted from one side through an open window on the back side, which can be closed by the aluminum covers. According to the operation experience and simulation result,[16] the extreme temperature at the magnet region can be higher than 200°C, induced by the heat deposition of coextracted electrons. On the other hand, the required remanence of the magnet is up to 1.1 Tesla (T) according to the ITER design.[11] After a market survey, Sm_2Co17 magnets were selected for the EG. Sm_2Co17 magnets have both the high values of magnetic energy product and good stability at high temperature (up to 300°C, according to the testing results of manufacturer). Besides, the electron deflection field also has a certain contribution to the filter field on the top surface of the PG.

III. MANUFACTURING PROCESS

The electrodeposition technique is one of the manufacturing methods for the grid system of the NBI ion source. Generally, the grids were manufactured by electrodeposition of copper onto a copper baseplate with premachined grooves for cooling channels and water manifolds, and then the apertures were milled. This process has been successfully applied to the half-size ITER beam source ($1 \times 0.9\ m^2$ with two segments) on the ELISE test facility at IPP-Garching,[18–20] and was recommended for the manufacturing of the full-size ITER beam source on the SPIDER and MITICA test facilities at Consorzio RFX (Refs. 21, 22, and 23). Deep-hole drilling is another common manufacturing method for the cooling channels of multiaperture grids of both positive and negative ion sources.[24,25] A rectangular-shaped cooling channel is more desired through multiple drillings. Due to having a larger cross section, the rectangular-shaped channel is expected to have a larger heat transfer area and a faster flow velocity than the circular-shaped channel.

Based on the production experience of ASIPP suppliers, a manufacturing process involving the vacuum brazing technique was proposed to fabricate all grids of the prototype negative ion source. The vacuum brazing technique has been widely used in fusion engineering and has a regular and strict technological process. Two prototype EGs were trial-produced by the Hefei Keye company in order to check the feasibility and reliability of this process. The details of the manufacturing process are shown in Fig. 3 and described as follows:

1. The ground copper plate was ultrasonically tested and machined to the designed size. The thickness and width of the plate were larger than the required value, to leave some spare for final precise machining.

2. Because the width of the magnet groove was narrower than the cooling channel, all the grooves for the cooling channels, manifolds, and magnets were milled from the front side of the ground plate. The steps between the magnet groove and cooling channel groove were available to place the cover. In addition, four tunnels connecting to the manifolds were drilled for the water inlet and outlet.

3. The cover for forming the cooling channels and manifolds, and the layers for separating the magnet grooves and the cooling channels, were manufactured,

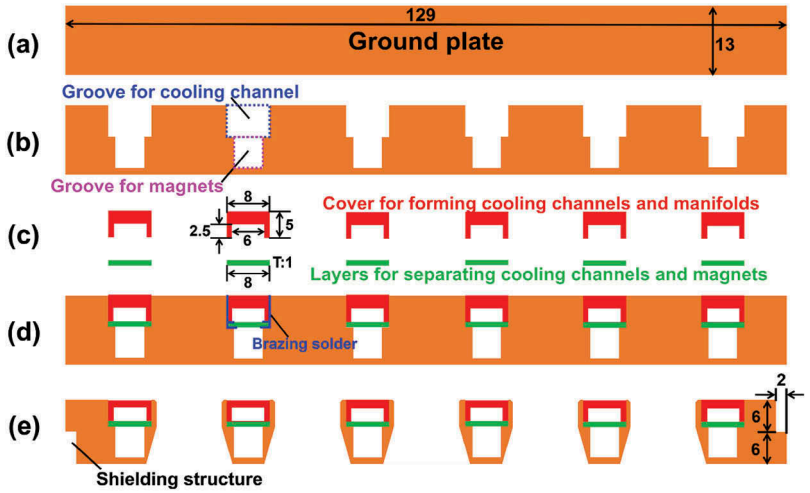

Fig. 3. Scheme of the manufacturing process for the prototype EGs.

respectively. The cover was one entity as shown in Fig. 4, and the layers were rectangular strips. Note that the prototypes had a difference from the original design. The two cooling channels were simplified to a large single one. The purpose of this change was to increase the reliability of the vacuum brazing in the next step.

4. The layers and the cover were joined with the ground plate through vacuum brazing. The brazing solder (brazing foils, $Ag_{72}Cu_{28}$) was mainly placed on the cover which had strict demands for cooling water. On the other hand, the brazing solder needed to be carefully controlled between the magnet grooves and layers, otherwise it would prevent the installation of the magnets. The water feedthroughs were brazed with the grid at the same time. The brazing performance was tested with the leak test and the thermal imaging test (see Sec. IV for details).

Fig. 4. Details of the cover for the manifolds and the cooling channels.

5. After passing the above tests, the final machining process was carried out. The spare thickness (thinned off from 13 mm to 12 mm), the shielding structure, the mounting holes, and the extraction apertures were milled. The crossing grooves (shown in Fig. 2) for inserting or observing the magnets were milled from the back side.

The finished prototype EGs are exhibited in Fig. 5.

As a whole, the first step was to fabricate a ground plate with the open grooves for the cooling circuit and magnets. The second step was to seal these open grooves

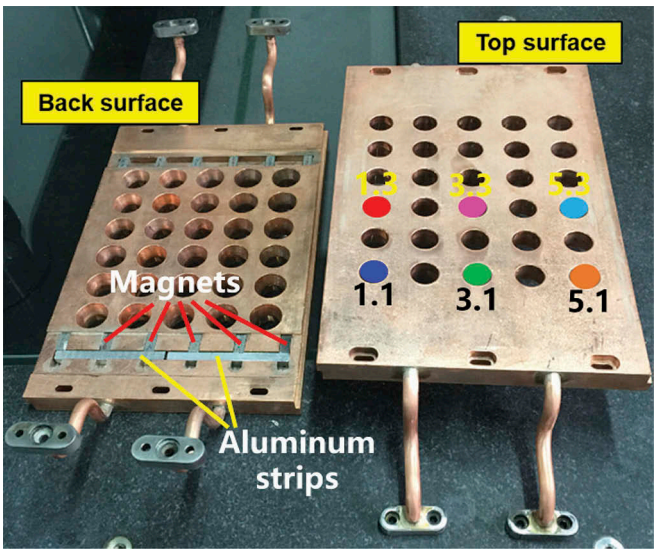

Fig. 5. Two prototype EGs of the prototype negative ion source (top and back views). The colorful circles represent the measured apertures in the magnetic test, and the number of apertures gives their row number and column number. Electron deflection magnets and aluminum strips are indicated.

with the matching covers through vacuum brazing. The last step was the precise manufacturing of the finished product conforming to the design requirements. Comparing the vacuum brazing method to the electrodeposition method, they have a similar manufacturing process except for the technique for covering the grooves.

IV. TESTING CAMPAIGN

Although there were no apparent defects on the prototype EGs, the feasibility and reliability of this manufacturing process was estimated through further tests.

IV.A. Dimension Inspection

All of the machining process was carried out on the computerized numerical control machine tool. Thus, the dimension precisions of the prototype EGs were guaranteed to meet the design requirement. The most uncertainty came from the brazing solder, which might round the corners of the magnet grooves and cooling channels. An endoscope was used to evaluate the inner-surface morphology of the magnet grooves from the openings. The results indicated that most of the brazing solder was deposited evenly; a screenshot is shown in Fig. 6. Some testing blocks with the same size of the magnets could be freely inserted into all the grooves.

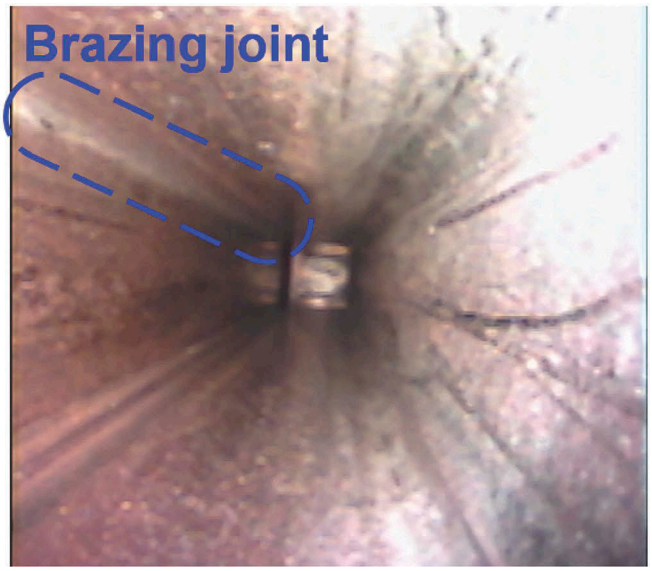

Fig. 6. Screenshot of the endoscope monitoring inside one magnet groove.

IV.B. Leak Tests

Before leaving the factory, the prototype EGs passed the common leak inspection (leak rate less than 10^{-10} Pa·m^3/s), where the internal cooling circuit was highly evacuated and connected to the leak detector. Then helium was sprayed over the grid, and the leak detector was used to detect the trace of helium to assess the leakage.

However, the working condition of the grids was quite different, where the external was a high vacuum but the internal was high pressure running water. Hence the leak tests of all grids were carried out by using a special device. This leak testing equipment has successfully exposed several undetectable leakages of the grids of the EAST-NBI ion source, as shown in Fig. 7. The testing equipment consists of a chamber, a vacuum pump, a leak detector, and a pressure adjustable helium tank.

The tested grid was placed inside the chamber where it was evacuated to ~10^{-1} Pa by the vacuum pump. One of the water feedthroughs of the grid was connected to the helium tank outside, and the other three water feedthroughs were sealed. Then the cooling circuit was evacuated through a branch connecting to the vacuum pump. A static helium pressure of 1 MPa was applied inside the cooling circuit for 10 min, and the leak detector connecting to the chamber was used to detect the quantity of spilled helium. The tests were passed with the helium leak rate less than 10^{-10} Pa·m^3/s (acceptable value), and there were no deformations on the surfaces.

IV.C. Thermal Imaging Tests

When it was determined that there were no leakages through the junctions, it had to be demonstrated that the cooling water could flow smoothly inside every cooling channel of the prototype EGs. According to the manufacturing experience of the grids for the EAST-NBI ion source, the cooling channels would obstruct easily if the brazing solder was not handled carefully. Because the cooling channels were close to the surface, thermal imaging tests were applied to assess the water flow status.

The main instruments used in the thermal imaging tests were an infrared thermal camera displaying the surface temperature and a water supply with two branches of different temperatures. The camera was handheld and manually focused on the top surface of the grid. The water flowed through the cooling circuit from the inlet to the outlet feedthroughs. The water was repetitively switched between the cold and hot branches. During the switch transition process, the temperature of the grid entity stayed the same, but the

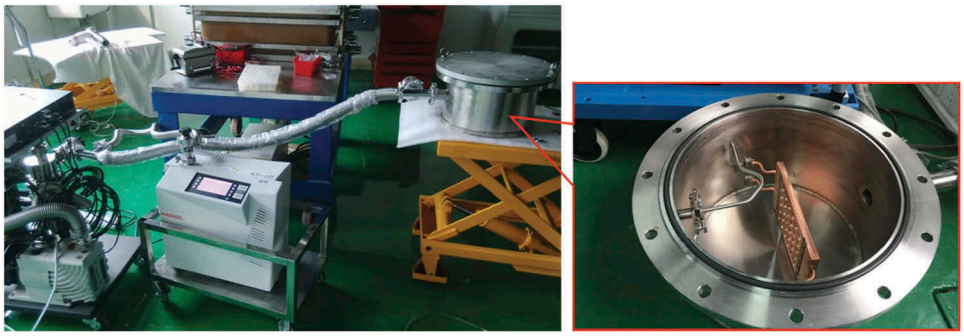

Fig. 7. Special leak testing equipment for the grids.

temperature of the region with the running water transformed rapidly, so that the clear cooling channels could be distinguished on the infrared thermal camera at the moment.

Two problems, however, arose in practice. One was that the copper grids had a reflective surface, which caused some overexposure regions of the camera image. A wet absorbing paper was suggested to apply on the revealing surface by the NBI team of Consorzio RFX (Ref. 22). In our case, the tests were carried out in the darkroom and the overexposure was suppressed. The other problem was that due to the high thermal conduction of copper, it hardly took a clear thermal image for all cooling channels at one time. Finally, through monitoring several switch transition processes of the water temperature, it was confirmed that no channel was obstructed in the two prototype grids.

Figure 8 shows an example of the thermal imaging tests. The four pictures are a time evolution of the grid surface temperature during one switch transition process. Two hot spots in Fig. 8a correspond to the two water inlets. The two channels near the two inlets became hot first, where the flow velocity was faster. Then, the hot region quickly spread over the whole surface, as shown in Fig. 8b. The other four channels can be faintly distinguished in Figs. 8c and 8d. All the thermal pictures are quite symmetric along the centerline of the grid, which indicates that all the channels were clear and consistent.

IV.D. Magnetic Tests

A measurement was carried out to measure the magnetic field along the centerlines of some typical apertures, as shown in Fig. 5. The same ASIPP supplier could only produce the Sm_2Co_{17} magnets with the average remanence of 1.05 T. A sampling showed that the

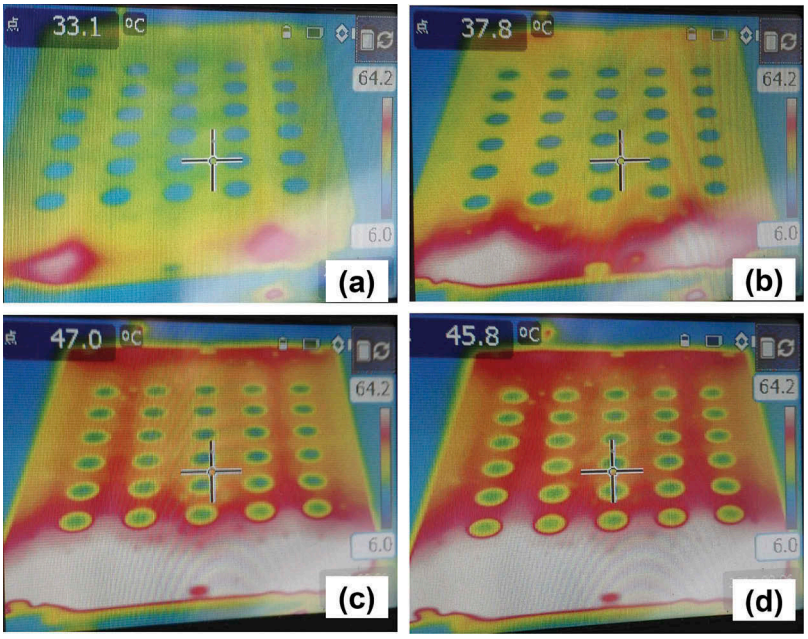

Fig. 8. Time evolution of thermal image during one switch transition process.

nonuniformity of the magnets is about ±5%. However, these magnets were still used for the prototype EGs in order to measure a real magnetic field and compare with the ideal simulation.

The dimensions of the electron deflection magnets were 5.5 × 5 × 20 mm (H × W × L), and seven magnets were inserted into each groove of the prototype EGs. There were large repulsive forces between the magnets in the same groove. It was suggested that the alternate rows of magnets with the same pole (e.g., north pole on the top surface) be inserted first, and then the magnets with the opposite pole (south pole on the top surface) could be easily inserted into the remaining grooves. The mounting slots were blocked off by two square aluminum strips, which were just squeezed and fixed by the repulsive forces of the magnets.

The magnetic testing equipment, shown in Fig. 9, is composed of a gaussmeter with a three-axis magnetic probe COLY Y08P150G93 and a coordinate measuring machine (CMM). Because the CMM was dedicated to the measurement and assembly of the ion source components, the magnetic probe was temporarily taped on the *z*-axis rocker. Meanwhile, the distribution of the magnetic field was simulated through the finite element method via ANSYS.

The calculation and measurement results of the magnetic field along the centerlines of six apertures are compared in Fig. 10. The calculation still considered the magnet remanence of 1.1 T, though the actual value was a little lower. On the whole, the measured data points had similar trends with the calculated profiles. More details are revealed in the zoom-in view near the peaks of the calculated profiles. Of course, the calculated peak in each aperture was larger than the corresponding measured one,

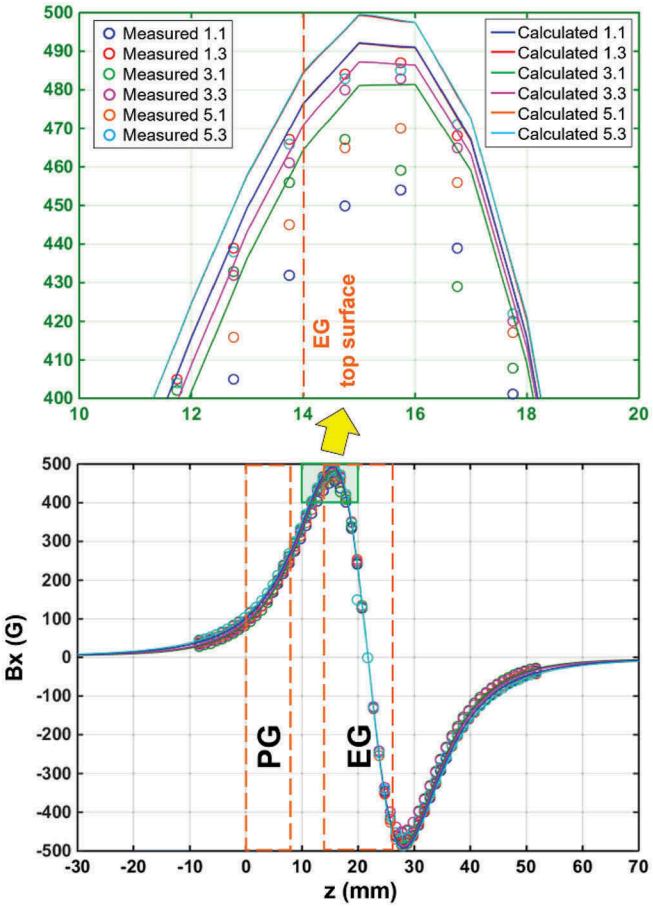

Fig. 10. Comparison between the calculated magnetic field and the measured results along the centerlines of typical apertures shown in Fig. 5. (a) Locally enlarged view of the region z [10, 20] and Bx [400, 500]. (b) Positions of PG and EG are displayed. The calculated profiles of 1.1 and 5.1, 1.3 and 5.3 are overlapping, respectively, due to the symmetry of the magnet arrangement.

Fig. 9. Magnetic testing equipment.

but the average measured peaks (473 G) were 3.9% lower than the calculated results (492 G). The actual strength could be acceptable during the preliminary experiment of low voltage (~5 kV) extraction. There were two nonuniformities of the magnetic field indicated through the calculation. Due to the edge effect of the magnet row, the magnetic field was lower at the edge aperture in the same row (e.g., aperture 1.3 > 1.1). The other one was that the edge row of the magnets had longer closed magnetic lines and larger magnetic flux, leading to the larger magnetic field in the apertures nearby (e.g., aperture 1.1 > 3.1 or 1.3 > 3.3). The measured results had similar features, but a certain degree of deviation (4.0%) was found, combined with the magnets' own nonuniformity. Note that all the calculated and measured peaks were located below the EG top surface.

V. CONCLUSION

Through cooperation with the ASIPP supplier, two multiaperture and multichannel copper grids have been constructed, which have a similar structure to the extraction grid of the prototype negative ion source. The premachined cooling channels and magnet grooves on the grid were formed by vacuum brazing the special layers and cover. Both of the grids passed the common inspections before leaving the factory.

However, a more stringent testing campaign was carried out to imitate the work conditions as closely as possible. As a result, the dimension inspections, leak tests, and thermographic flow tests were successful for both grids. The related manufacturing method is recommended for the construction of all grids, although in the two prototype grids the single large cooling channel between two rows of apertures substituted for the separated two channels. This method can be applied to the molybdenum-made plasma grid, which has been proved in the construction of grids for the EAST-NBI ion source.

The average remanence (1.05 T) of the Sm_2Co17 magnets from the same supplier is less than the required value (1.1 T). The measured magnetic fields along the aperture centerline have similar profiles with the calculated results, but a certain degree of deviations (with a maximum field nonuniformity of 4.0%) was found, combined with the magnets' own nonuniformity. The average measured peaks (473 G) are 3.9% lower than the calculated results (492 G). The actual strength can be acceptable.

Acknowledgments

The authors are much indebted to the other members of EAST NBI group for their continuous encouragement and support. This work was supported by the National Natural Science Foundation of China under grants 11505224, 11575240, and 11405207; the International Science and Technology Cooperation Program of China under grant 2014DFG61950; and the Foundation of ASIPP under grant DSJJ-14-JC07.

References

1. B. N. WAN et al., "Physics Design of CFETR: Determination of the Device Engineering Parameters," *IEEE Trans. Plasma Sci.*, **42**, 495 (2014); https://doi.org/10.1109/TPS.2013.2296939.
2. Y. T. SONG et al., "Concept Design of CFETR Tokamak Machine," *IEEE Trans. Plasma Sci.*, **42**, 503 (2014); https://doi.org/10.1109/TPS.2014.2299277.
3. J. L. WEI et al., "Design of the Prototype Negative Ion Source for Neutral Beam Injector at ASIPP," *Plasma Sci. Technol.*, **18**, 954 (2016); https://doi.org/10.1088/1009-0630/18/9/13.
4. Y. H. XIE et al., "Development and Preliminary Results of Radio Frequency Ion Source," *Rev. Sci. Instrum.*, **87**, 02B302 (2016); https://doi.org/10.1063/1.4931786.
5. C. D. HU et al., "Performance of Positive Ion Based High Power Ion Source of EAST Neutral Beam Injector," *Rev. Sci. Instrum.*, **87**, 02B301 (2016); https://doi.org/10.1063/1.4931709.
6. C. D. HU et al., "Overview of Development Status for EAST-NBI System," *Plasma Sci. Technol.*, **17**, 817 (2015); https://doi.org/10.1088/1009-0630/17/10/02.
7. C. D. HU, "First Achievement of Plasma Heating for EAST Neutral Beam Injector," *Plasma Sci. Technol.*, **17**, 1 (2015); https://doi.org/10.1088/1009-0630/17/1/01.
8. Y. H. XIE et al., "The R&D Progress of 4 MW EAST-NBI High Current Ion Source," *Rev. Sci. Instrum.*, **85**, 02B315 (2014); https://doi.org/10.1063/1.4831747.
9. L. SCHIESKO et al., "Caesium Influence on Plasma Parameters and Source Performance During Conditioning of the Prototype ITER Neutral Beam Injector Negative Ion Source," *Plasma Phys. Controlled Fusion*, **53**, 085029 (2011); https://doi.org/10.1088/0741-3335/53/8/085029.
10. J. L. WEI et al., "Conceptual Design of Magnetic Filter for the Prototype Negative Ion Source at ASIPP," *Fusion Eng. Des.*, **113**, 23 (2016); https://doi.org/10.1016/j.fusengdes.2016.10.005.
11. H. P. L. DE ESCH et al., "Physics Design of the HNB Accelerator for ITER," *Nucl. Fusion*, **55**, 096001 (2015); https://doi.org/10.1088/0029-5515/55/9/096001.
12. A. KOJIMA et al., "Achievement of 500 keV Negative Ion Beam Acceleration on JT-60U Negative-Ion-Based Neutral Beam Injector," *Nucl. Fusion*, **51**, 083049 (2011); https://doi.org/10.1088/0029-5515/51/8/083049.
13. Y. TAKEIRI et al., "High Performance of Neutral Beam Injectors for Extension of LHD Operational Regime," *Fusion Sci. Technol.*, **58**, 482 (2010); https://doi.org/10.13182/FST10-A10834.
14. T. S. KIM et al., "Performance of a New Ion Source for KSTAR Tokamak Plasma Heating," *Plasma Sci. Technol.*, **16**, 620 (2014); https://doi.org/10.1088/1009-0630/16/6/15.
15. R. NOCENTINI et al., "Optimization of the Cooling Circuit and Thermo-Mechanical Analysis for the Extraction Grid of ELISE," *Fusion Eng. Des.*, **86**, 916 (2011); https://doi.org/10.1016/j.fusengdes.2011.01.147.
16. M. KASHIWAGI et al., "Development of Negative Ion Extractor in the High-Power and Long-Pulse Negative Ion Source for Fusion Application," *Rev. Sci. Instrum.*, **85**, 02B320 (2014); https://doi.org/10.1063/1.4852297.

17. P. AGOSTINETTI et al., "Physics and Engineering Design of the Accelerator and Electron Dump for SPIDER," *Nucl. Fusion*, **51**, 063004 (2011); https://doi.org/10.1088/0029-5515/51/6/063004.

18. B. HEINEMANN et al., "Design of the 'Half-Size' ITER Neutral Beam Source for the Test Facility ELISE," *Fusion Eng. Des.*, **84**, 915 (2009); https://doi.org/10.1016/j.fusengdes.2008.11.076.

19. B. HEINEMANN et al., "Negative Ion Test Facility ELISE—Status and First Results," *Fusion Eng. Des.*, **88**, 512 (2013); https://doi.org/10.1016/j.fusengdes.2012.11.003.

20. R. NOCENTINI et al., "Toward a Large RF Ion Source for the ITER Neutral Beam Injector: Overview of the ELISE Test Facility and First Results," *IEEE Trans. Plasma Sci.*, **42**, 616 (2014); https://doi.org/10.1109/TPS.2013.2293607.

21. P. AGOSTINETTI et al., "Investigation of the Thermo-Mechanical Properties of Electro-Deposited Copper for ITER," *J. Nucl. Mater.*, **417**, 924 (2011); https://doi.org/10.1016/j.jnucmat.2011.01.084.

22. P. AGOSTINETTI et al., "Manufacturing and Testing of Grid Prototypes for the ITER Neutral Beam Injectors," *IEEE Trans. Plasma Sci.*, **42**, 628 (2014); https://doi.org/10.1109/TPS.2013.2296743.

23. M. PAVEI et al., "Manufacturing of the Full Size Prototype of the Ion Source for the ITER Neutral Beam Injector—The SPIDER Beam Source," *Fusion Eng. Des.*, **96–97**, 319 (2015); https://doi.org/10.1016/j.fusengdes.2015.07.013.

24. G. Q. ZOU et al., "Study of Ion Beam Extraction Elements for HL-2M Neutral Beam Injector," *Proc. 40th EPS Conf. on Plasma Physics*, Espoo, Finland, July 1–5, 2013, Vol. 37D, p. P1.140, Europhysics Conference Abstracts (2013).

25. D. W. LEE et al., "Assessment and Modification of an Ion Source Grid Design in KSTAR Neutral Beam System," *Rev. Sci. Instrum.*, **85**, 02B306 (2014); https://doi.org/10.1063/1.4826336.